# Transition Radiation Detector study

A. Andronic

*Gesellschaft für Schwerionenforschung, Darmstadt, Germany*

**Abstract**

The basic features of the transition radiation and how they are used for the design of a Transition Radiation Detector (TRD) are presented. The emphasis is put on the design of a TRD for the ALICE experiment at LHC.

## 1 Introduction

Predicted in 1946 by Ginzburg and Frank [1], the transition radiation (TR) phenomenon had to wait quite a long time since it was successfully observed experimentally and applied for the identification of particles, especially when it was realized that under some conditions the spectrum of emitted radiation extends into the X-rays domain [2]. Since then many studies have been done, both at the basic [3, 4, 5, 6] and applicative [4, 7, 8, 9, 10, 11, 12, 13, 14] level. Consequently, TRDs were used or are now being used in a multitude of experiments: UA2 [15], ZEUS [16], NA31 [17], PHENIX [18, 19], HELIOS [20], DØ [21, 22], kTeV [23], H1 [24, 25], WA89 [26], MACRO [27], ATLAS [28], NOMAD [29], HERMES [30], mainly for electron-pion separation.

The subject was comprehensively reviewed in ref. [20].

## 2 Generalities

The practical theory of the TR production is presented in ref. [4, 5, 6]. Here I briefly summarize the most important results.

The double differential energy spectrum radiated by a charged particle with the Lorentz factor $\gamma$ traversing an interface between two dielectric media (with the dielectric constants $\epsilon_1$ and $\epsilon_2$) has the following expression:

$$\frac{\mathrm{d}^2W}{\mathrm{d}\omega\mathrm{d}\Omega} = \frac{\alpha}{\pi^2}\left(\frac{\theta}{\gamma^{-2}+\theta^2+\xi_1^2} - \frac{\theta}{\gamma^{-2}+\theta^2+\xi_2^2}\right)^2 \tag{1}$$

deduced for: $\gamma \gg 1$, $\quad \xi_1^2, \xi_2^2 \ll 1$, $\quad \theta \ll 1$. $\xi_i^2 = \omega_{Pi}^2/\omega^2 = 1 - \epsilon_i(\omega)$, $\omega_{Pi}$ is the (electron) plasma frequency for the two media and $\alpha$ is the fine structure constant ($\alpha$=1/137). The plasma frequency is a material property and has the following expression:

$$\omega_P = \sqrt{\frac{4\pi\alpha n_e}{m_e}} = 28.8\sqrt{\rho\frac{Z}{A}} \quad \text{eV} \tag{2}$$

where $n_e$ and $m_e$ are the electron density and mass. Typical values for plasma frequency are $\omega_P^{CH_2}$=20 eV, $\omega_P^{Air}$=0.7 eV.

As the emission angle of the TR is small ($\simeq 1/\gamma$) one usually integrates over the solid angle and gets the (differential) energy spectrum:

$$\left(\frac{\mathrm{d}W}{\mathrm{d}\omega}\right)_{interface} = \frac{\alpha}{\pi}\left(\frac{\xi_1^2 + \xi_2^2 + 2\gamma^{-2}}{\xi_1^2 - \xi_2^2}\ln\frac{\gamma^{-2} + \xi_1^2}{\gamma^{-2} + \xi_2^2} - 2\right) \tag{3}$$

For a foil one has to sum up the contributions of the two interfaces, ending with the expression:

$$\left(\frac{\mathrm{d}^2W}{\mathrm{d}\omega\mathrm{d}\Omega}\right)_{foil} = \left(\frac{\mathrm{d}^2W}{\mathrm{d}\omega\mathrm{d}\Omega}\right)_{interface} \times 4\sin^2(\phi_1/2) \tag{4}$$

where $4\sin^2(\phi_1/2)$ is the interference factor. The above spectra are plotted for one interface and for one foil in Fig. 1 (same parameters as in [4]).

For a stack of $N_f$ foils of thickness $l_1$, separated by a medium (usually a gas) of thickness $l_2$, one has:

$$\left(\frac{\mathrm{d}^2W}{\mathrm{d}\omega\mathrm{d}\Omega}\right)_{stack} = \left(\frac{\mathrm{d}^2W}{\mathrm{d}\omega\mathrm{d}\Omega}\right)_{foil} \times \exp\left(\frac{1 - N_f}{2}\sigma\right)\frac{\sin^2(N_f\phi_{12}/2) + \sinh^2(N_f\sigma/4)}{\sin^2(\phi_{12}/2) + \sinh^2(\sigma/4)} \tag{5}$$

where $\phi_{12} = \phi_1 + \phi_2$ is the phase retardation, $\phi_i \simeq (\gamma^{-2} + \theta^2 + \xi_i^2)\omega l_i/2$ and $\sigma = \sigma_1 + \sigma_2$ is the total absorption cross section for the radiator (foil + gas).
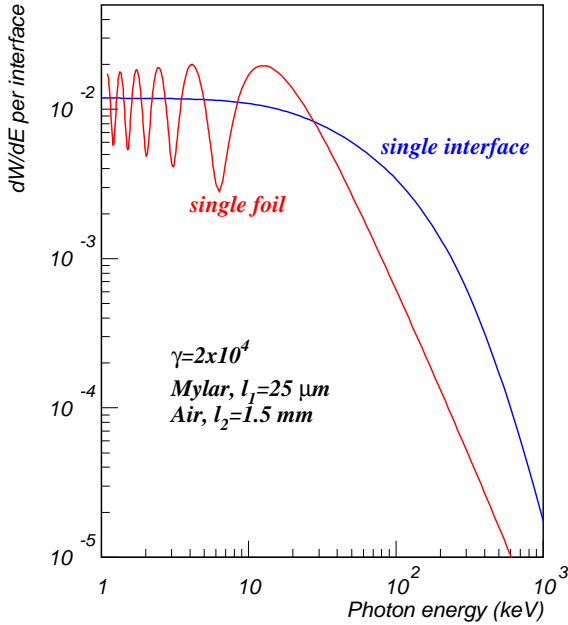


Figure 1: TR spectrum for single interface and single foil configurations.
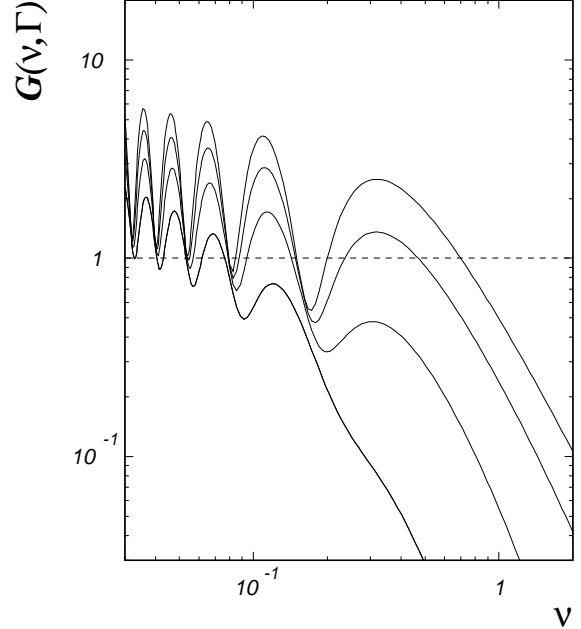


Figure 2: Function $G(\nu, \Gamma)$.

The TR produced by a multifoil radiator can be characterized by the following qualitative features:

- one can define the so-called "formation zone": $Z_i = (\gamma^{-2} + \xi_i^2)^{-1}2/\omega$, which is interpreted as the distance after which the separation between particle and emitted photon

is of the order of photon wavelength [4]. The yield is supressed if $l_i \ll Z_i$ and this is what is called "formation zone effect".

In the case of constructive interference one has:

$$\left(\frac{\mathrm{d}^2W}{\mathrm{d}\omega\mathrm{d}\Omega}\right)_{foil} = 2 \times \left(\frac{\mathrm{d}^2W}{\mathrm{d}\omega\mathrm{d}\Omega}\right)_{interface} \quad ; \quad \left(\frac{\mathrm{d}^2W}{\mathrm{d}\omega\mathrm{d}\Omega}\right)_{stack} = N_f \times \left(\frac{\mathrm{d}^2W}{\mathrm{d}\omega\mathrm{d}\Omega}\right)_{foil} \tag{6}$$

- the TR spectrum has the most relevant maximum at: $\omega_{max} = l_1\omega_{P1}^2/2\pi$ and this allows the "tuning" of TRD by varying the material and thickness of the radiator foils

- for $l_2/l_1 \gg 1$ the TR spectrum is mainly determined by the single foil interference

- the multiple foil interference governs the saturation at high $\gamma$, above the value:

$$\gamma_s = \frac{1}{4\pi}\left[(l_1 + l_2)\omega_{P1} + \frac{1}{\omega_{P1}}(l_1\omega_{P1}^2 + l_2\omega_{P2}^2)\right] \tag{7}$$

A convenient way to study the TR features is to use scaled variables [5]:

$$\Gamma = \gamma/\gamma_1, \quad \nu = \omega/\omega_1 \tag{8}$$

where $\gamma_1 = l_1\omega_{P1}/2, \quad \omega_1 = \gamma_1\omega_{P1}$. In terms of the above variables, the TR production of a foil can then be written as:

$$\left(\frac{\mathrm{d}W}{\mathrm{d}\omega}\right)_{foil} = \frac{2\alpha}{\pi}G(\nu,\Gamma) \tag{9}$$

The function $G(\nu,\Gamma)$ is plotted in Fig. 2 for several values of the $\Gamma$ parameter (0.5, 1, 2, 4).
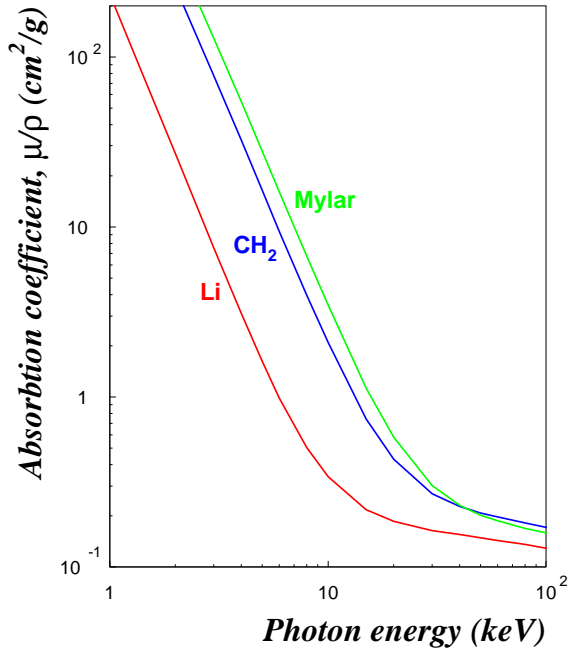


Figure 3: X-rays absorption coefficient for Li, CH$_2$ and mylar.
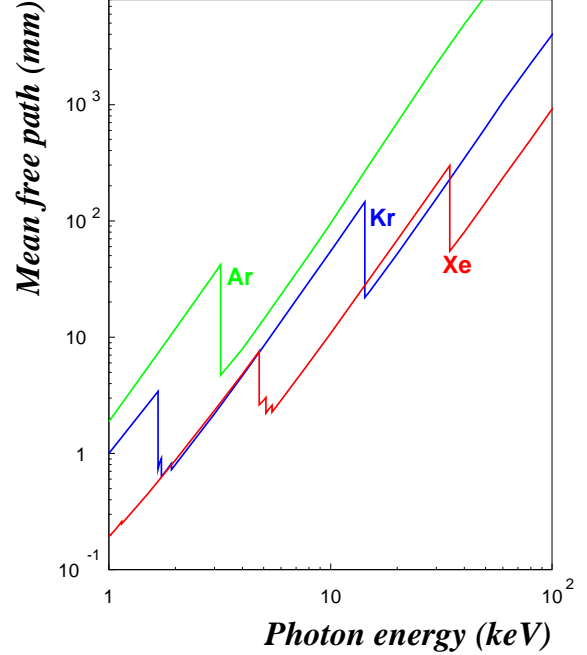


Figure 4: Mean free path of X-rays in different gases.

Taken into account the above features it is evident that a TRD requires a careful optimization concerning the following aspects:

- radiator:

  - *type:* regular (foils) vs. random (foams, fibers). The foil radiators were proven to be better than foams [18], but the fibers were measured to give a similar performance compared to foils [7, 14, 32, 33, 16, 34, 24, 23, 30]

  - *material:* as foil a material with as low X-rays absorption coefficient as possible. Li [10], Be, polypropylene - $CH_2$ [19, 29], mylar [4] have been used (see Fig. 3 for the differences in the absorption coefficient for Li, $CH_2$ and mylar). For the gap a gas is used, preferrably He [25] for the low absorption cross section, but due to He inconveniencies, air [19], $N_2$ [29] or $CO_2$ [17] are most commonly used

  - *configuration:* foil and gap thicknesses - $l_1$, $l_2$ (or $d_1$, $d_2$) and number of foils - $N_f$

- detector:

  - *gas* type and thickness ($x$), see ref. [20, 31] for a comprehensive discussion on this issue. Fig. 4 shows the mean free path as a function of photon energy for the gases used normally in the X-rays detectors

  - *read-out* and signal processing (total charge detection - "Q" [17, 26, 29, 30], cluster counting - "N" [16, 20, 28] or FADC [33, 34, 24, 15, 16, 22, 25], which allows to use both "Q" and "N" for TR recognition

- number of layers (N)
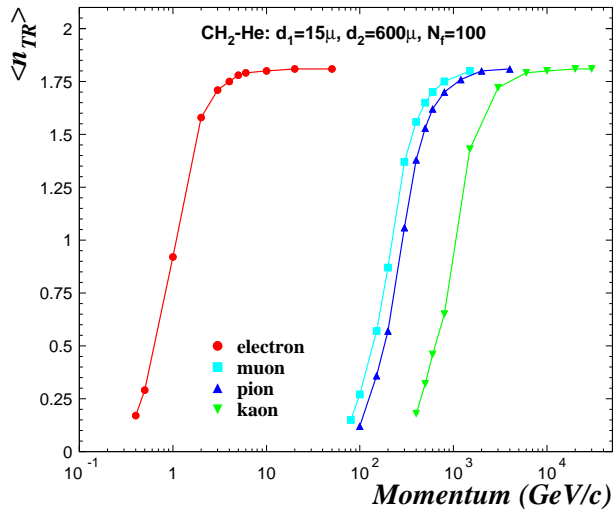


Figure 5: Momentum dependence of TR production for electrons, muons, pions and kaons.
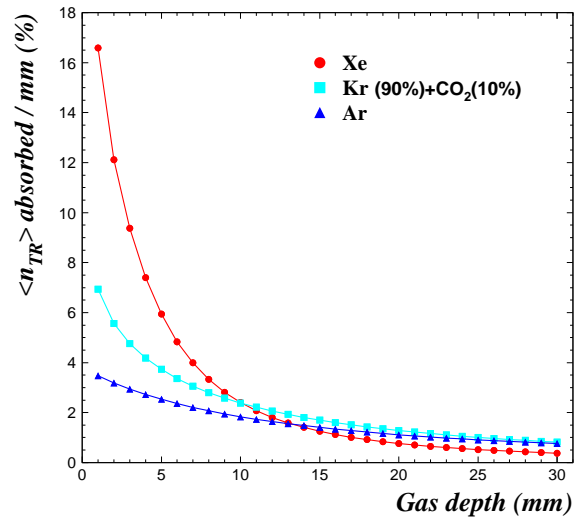
Figure 6: The fraction of absorbed TR photons as a function of detector depth.

How the transition radiation can be used to identify the particles can be understood from Fig. 5, where the momentum dependence of TR production is shown for electrons, muons, pions and kaons. Due to the dependence of TR on $\gamma$, it is evident that there is a big momentum range (1–100 GeV/c) where the electrons are the only particles producing

transition radiation. The kaons can also be disentangled from pions on the basis of TR in a certain momentum range (roughly 100–700 GeV/c) and $\pi/\Sigma$ identification has been done as well [26].

Fig. 6 shows the percentage of the average number of TR photons absorbed in each millimetre of the detector gas, for Xe, Kr and Ar mixtures. It is evident that in order to have a good detection efficiency a heavy gas has to be chosen.

The Table 1 presents a selection of configurations and performances of TRDs used by different experiments.

| Experiment [Ref.] | L (cm) / N | Radiator | Detector ($x$-cm) | Meth. | R / Eff. (%) |
|---|---|---|---|---|---|
| **ZEUS** [16] | 40 / 4 | $CH_2$ fibres | Xe-He-$CH_4$(1) | FADC | 2 / 90 |
| **NA31** [17] | 96 / 4 | $CH_2$-$CO_2$ | Xe-He-$CH_4$(2.5) | Q | 1.4 / 90 |
| **HELIOS** [20] | 70 / 8 | $CH_2$-Air | Xe-$C_4H_{10}$(1.8) | N | 0.05 / 90 |
| **D$\emptyset$** [22] | 33 / 3 | $CH_2$-$N_2$ | Xe-$CH_4$(2.3) | FADC | 20 / 90 |
| **H1** [25] | 60 / 3 | $CH_2$-He-$C_2H_6$ | Xe-He-$C_2H_6$(6) | FADC | 10 / 90 |
| **WA89** [26] ($\pi/\Sigma$) | 85 / 10 | $CH_2$ fibres | Xe-$CH_4$(0.8) | Q | 5 / 82 |
| **ATLAS** [28] | 78 / 16 | $CH_2$ | Xe-$CH_4$-$CO_2$(0.4) | N | 0.5 / 90 |
| **NOMAD** [29] | 90 / 9 | $CH_2$-$N_2$ | Xe-$CO_2$(1.6) | Q | 0.1 / 90 |
| **HERMES** [30] | 54 / 6 | $CH_2$ fibres | Xe-$CH_4$(2.54) | Q | 0.07 / 90 |
| **kTeV** [23] | 144 / 8 | $CH_2$ fibres | Xe-$CO_2$(2.9) | Q | 0.4 / 90 |
| **PHENIX** [19] | 60 / 6 | $CH_2$-$CO_2$ | Xe-$CH_4$(1.8) | Q | 1 / 90 |

Table 1: TRD characteristics used in some experiments.
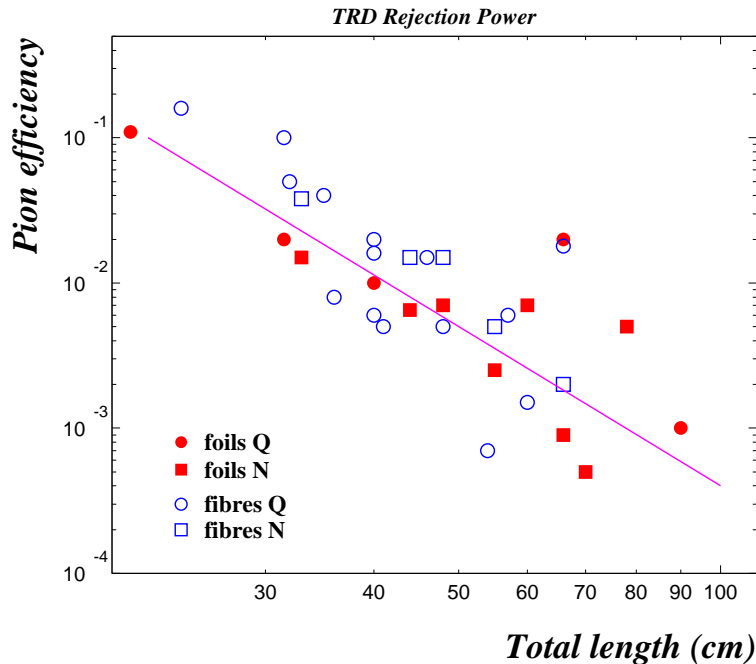


Figure 7: TRD rejection power as function of the total length of the detector.

Fig. 7 shows the rejection power of TRD vs. its total length [24, 20, 39] for the configurations presented in the above table and where the ones in ref. [13, 14, 15, 21, 24, 32, 33, 34] were added as well. The line is drawn to guide the eye. In most of the cases the momentum range was below 10 GeV/c. Although there is a clear improvement of the rejection power when the length of the detector increases, the performance of a TRD depends also on the configuration and signal processing (most of the results have been obtained using the likelihood method, one clear exception is the low rejection factor of 2% at 66 cm obtained using a simple charge sum criterion [13]). No relevant difference is observed between charge ("Q") and cluster counting ("N") methods [20].

It is also evident that the fibre solution is comparable to the foil in terms of performance vs. length [16, 34], although it can be worse in terms of total amount of material, and this is in some cases (as for ALICE) important.

It is worth spending a warning here about the worse "real life" TRD performances compared to test results [20], see also the DØ [22, 21] and H1 [25, 24] examples.

## 3 Method

In ref. [7] the TR has been studied for different (foil) radiator configurations. The incident electron was deflected by a magnet and the TR photons were detected by a semiconductor detector. The configuration of that experiment and measured spectra are shown in Fig. 8 a) and b-d) (where $a$ is the foil thickness), respectively.
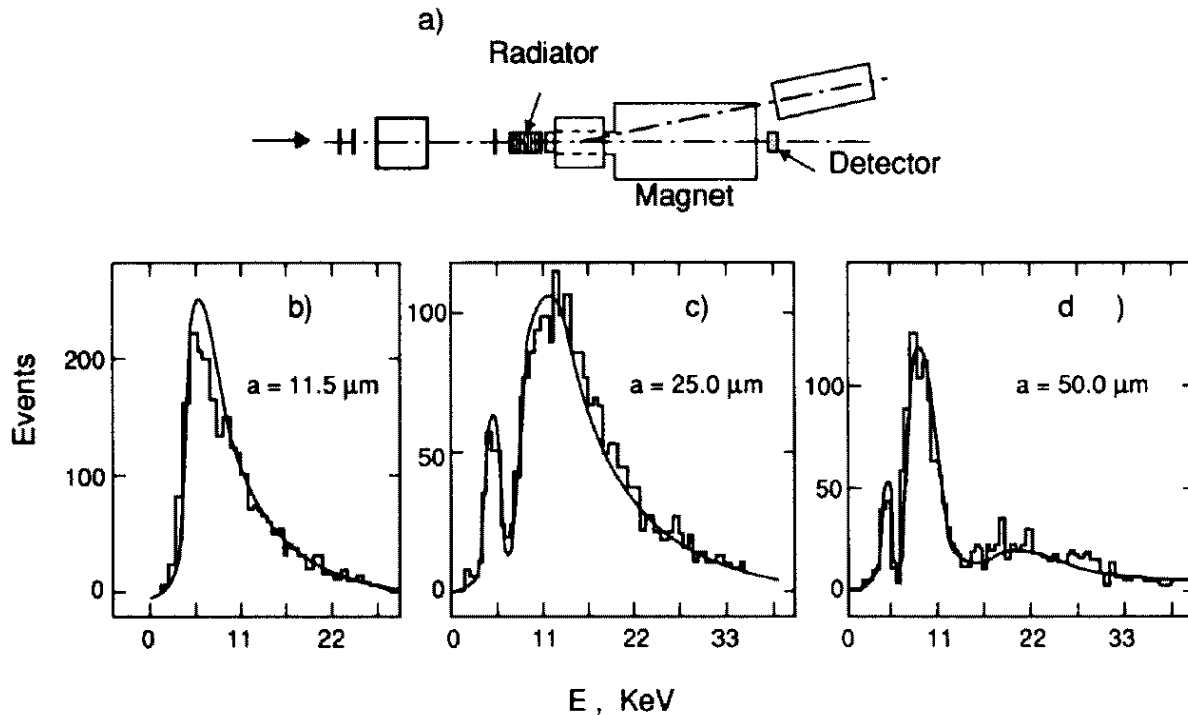


Figure 8: Experimental setup and results from TR study of ref. [7].

The smooth lines in this figure are the result of a calculation using a simpler expression

for the TR production:

$$\frac{dW}{d\omega} = \frac{4\alpha}{\sigma(\kappa+1)}(1 - \exp(-N\sigma)) \times \sum_n \theta_n \left(\frac{1}{\rho_1 + \theta_n} - \frac{1}{\rho_2 + \theta_n}\right)^2 [1 - \cos(\rho_1 + \theta_n)] \quad (10)$$

where:

$$\rho_i = \omega l_1/2c(\gamma^{-2} + \xi_1^2), \quad \kappa = l_2/l_1, \quad \theta_n = \frac{2\pi n - (\rho_1 + \kappa\rho_2)}{1+\kappa} > 0 \quad (11)$$

The above formulas are used for the present study as well and the next results are intended to test the present calculations against previous calculations and measurements, as well as for evidencing the main features of the TR production.
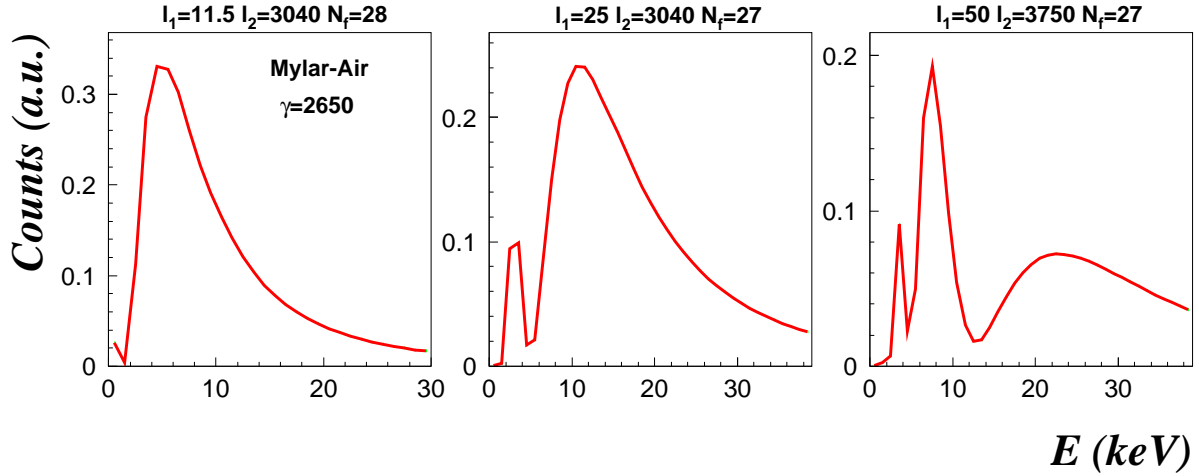


Figure 9: Present calculation of TR spectra for the configuration of ref. [7].

Fig. 9 presents the results of the present simulation obtained for the configuration of ref. [7]. The agreement is good and one can directly read the mentioned dependence of TR on the foil thickness.

Fig. 10 presents the average number of TR photons as a function of Lorentz factor $\gamma$ for the NOMAD configuration ($CH_2$ - $d_1$=15 $\mu$m, $N_2$ - $d_2$=250 $\mu$m, $N_f$=315, 1.6 cm Xe-90% + $CO_2$-10%) [38] and momentum for the PHENIX configuration ($CH_2$ - $d_1$=15 $\mu$m, air - $d_2$=818 $\mu$m, $N_f$=120, 1 cm Xe-95% + $C_4H_{10}$-5%) [18] and here the agreement is also reasonably good.

In both these figures one can notice again the threshold behaviour of the TR production and that the production becomes sizeable at values of $\gamma$ around 1000. Nevertheless, the TR production has been measured for values of $\gamma$ as low as 200, using many and very thin radiator foils [8].

Fig. 11 shows the dependence of the average value of TR energy deposited in the gas detector as a function of foil and gap thickness. The open points are the measured values from ref. [4]. Due to the formation zone effect, the TR yield is increasing as a function of
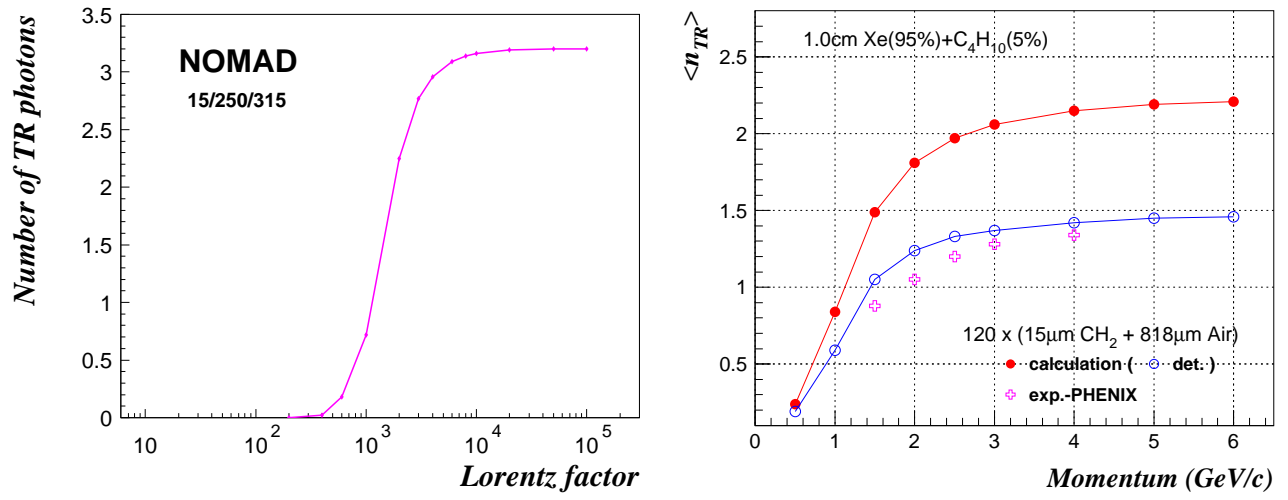
Figure 10: The average number of TR photons as a function of electron Lorentz factor $\gamma$ for the NOMAD configuration [38] and momentum for the PHENIX configuration [18].

foil and gap thickness reaching a saturation. In the case of foil, the yield starts to decrease at some point due to the dominant role of the absorption. The disagreement in the case of Kr might be explained by the escape of $K$ fluorescence photons (more important for Kr compared to Xe), neglected in the present calculations.
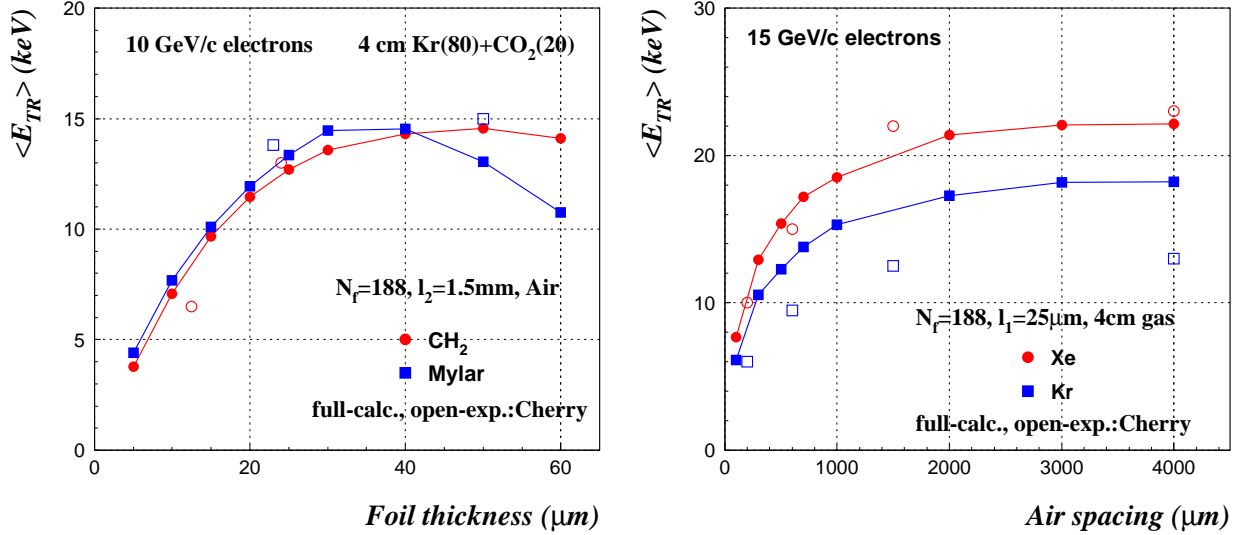


Figure 11: The average value of TR energy as a function of foil and gap thickness. The open points are the measured values from ref. [4].

For the present study the incidence of particles is supposed to be perpendicular to the radiator and gas chamber. The present simulation is done along the lines of ref. [35, 36, 37, 38].

To study to which extent the drift time information can be useful for the pion rejection, especially having in mind the contribution of delta-rays to the pion misidentification, a microscopic simulation of the energy loss in the drift chamber (TEC) has been performed.

The pulse shape (in terms of electrons before the gas amplification) as a function of drift time is depicted schematically in Fig. 12 for a typical collection of six "events", containing one electron and one pion of 3 GeV/c momentum each. It shows, for both particles, the energy loss by ionization and, in case of electrons, marked by the dots, the superimposed signal due to the absorption of TR photons. The gas gain fluctuations were taken into account, assuming a Yule-Furry distribution:

$$f(n) = \frac{1}{\bar{n}} \exp(-\frac{n}{\bar{n}}) \tag{12}$$

with $\bar{n}$=1000. An electronic noise of gaussian type ($\sigma$=1000 electrons) was randomly added in each time bin. The diffusion along the drift path, have been taken into account as well (the values of the logitudinal drift constant were obtained from GARFIELD, 170 $\mu$m/$\sqrt{cm}$, in the case of the $Xe/C_4H_{10}$ gas mixture and 330 $\mu$m/$\sqrt{cm}$ for $Xe/CO_2$). No charge loss due to shaping or charge sharing by the readout pads was considered.
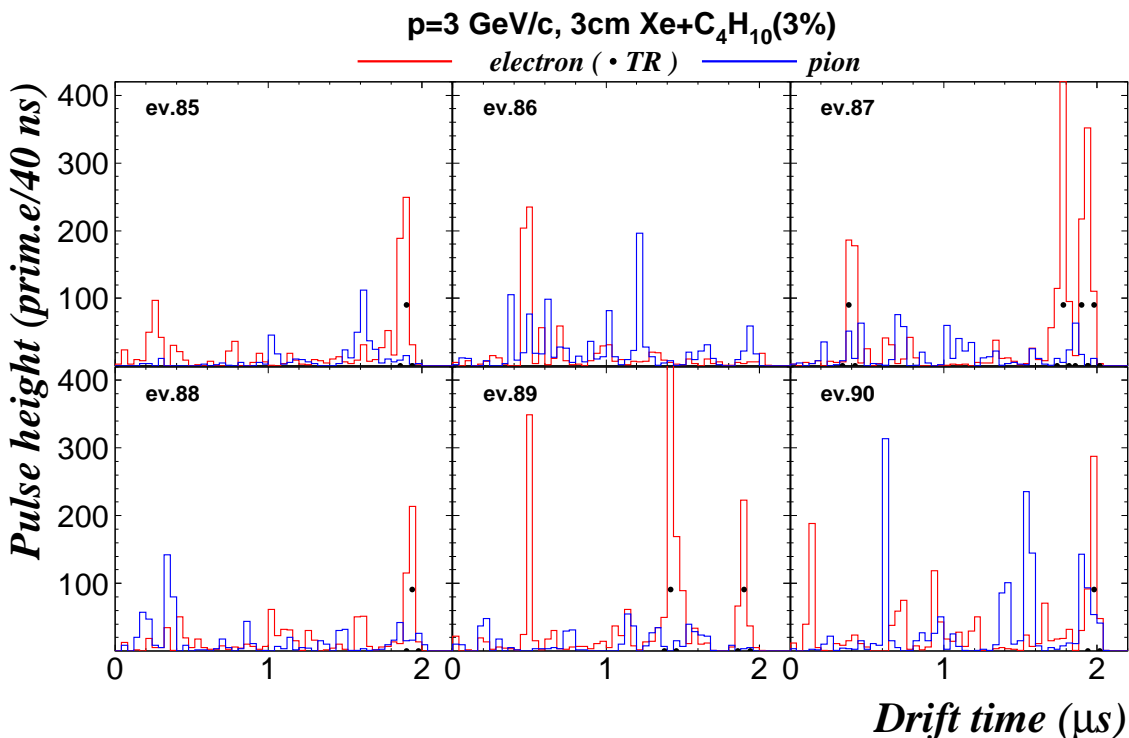


Figure 12: A sample of signals produced by electrons and pions passing one TRD layer.

Since for xenon there are no measurements concerning the cluster size distribution, we were bound to use a model for the delta-ray spectrum. The photo-absorption and ionization model (PAI) [40] has been intensively used for such studies [41, 42]. For the present simulations we adopted a parametrization of ref. [41] that gives reasonable values for the average ionization energy loss. This parametrization is presented in Fig. 13 along with the one obtained from GEANT [43] and the $1/E^2$ distribution, often used in such studies [44]. Plotted is the integral distribution:

$$\left(\frac{dN}{dx}\right)_{>E} = \int_E^\infty \frac{d^2N}{dxdE'}dE' \tag{13}$$

which represents the probability to have, per centimeter, a certain number of inelastic collisions with an energy transfer greater than $E$. Naturally, this distribution starts at the value of the lowest ionization potential, which for Xe is $I$=12.1 eV. These distributions correspond to MIP, namely $\gamma$=4. To have them for other values, one simply scales the number of primary collisions, $n_{prim}$ according to the Bethe-Bloch formula, taking into account the relativistic rise and the density effect (the upper limit of the delta-ray spectrum, determined by the kinematics, changes as well, but this is a minor effect). Fig. 14 shows the corresponding scaling factors for Ar, Kr and Xe, as extracted from GEANT. Note that the ecaling factor for the number of primary encounters is different than the one for the most probable value of the energy loss [42], most oftenly quoted in the litterature.
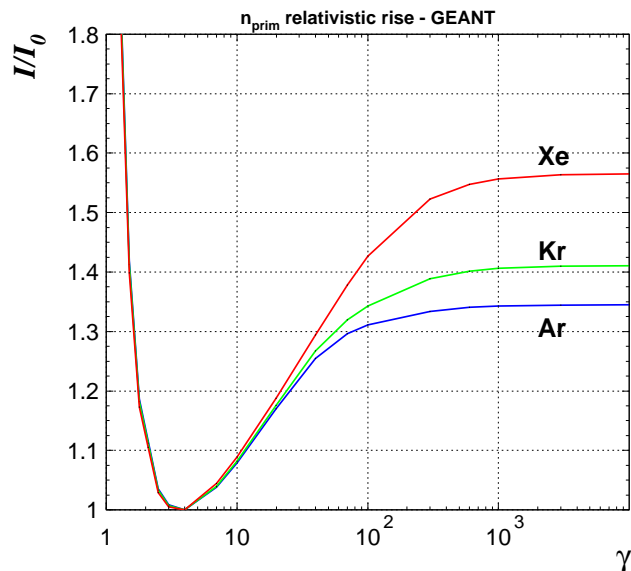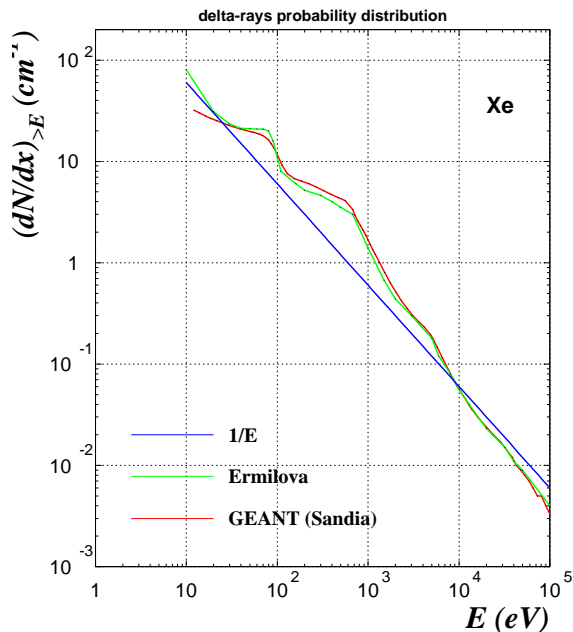


Figure 13: Delta-ray distribution probability.   Figure 14: Relativistic rise of the number of primary collisions.

As illustrated in Tables 2 and 3, both the value of $n_{prim}$ and the factor at the Fermi plateau differ quite substantially for different works available in litterature. For the present study we used the values from GEANT for the scaling factor.

|     | GEANT | Sauli | Ermilova |
|-----|-------|-------|----------|
| Ar  | 28    | 29    | 29       |
| Kr  | 28    | 22    | 35       |
| Xe  | 20.5  | 44    | 48       |

Table 2: $n_{prim}$ at $\gamma$=4.

|     | GEANT | Ermilova | Piuz |
|-----|-------|----------|------|
| Ar  | 1.34  | 1.39     | 1.32 |
| Kr  | 1.41  | 1.41     | -    |
| Xe  | 1.56  | 1.36     | -    |

Table 3: $n_{prim}$ - F.plateau/MIP($\gamma$=4).

The primary electrons produce secondary electrons according to the average energy necessary to produce one free electron, $W \simeq 22$ eV for Xe. These secondary electrons are located on the same position as the primary ones (note that the range of a 10 keV electron in Xe

is 0.5 mm), and the drift towards the amplification region, diffusion taken into account as mentioned already. See e.g. [45] for all the above details concerning drift chambers.

The effects of particles produced by secondary interactions will make the identification power decrease. These contributions, not taken into account here, will need a separate study.

# 4 Results

The optimization done here comprises a one module optimization, in terms of both radiator and detector configuration and a multimodule setup optimization, this last section looking at the pion misidentification as electron (or "pion efficiency" or "rejection power"). All the results presented are obtained for foils radiator, considering polypropylene ($CH_2$) as foil material.

To optimize a module of the TRD one has usually to maximize the production of the TR taking into account the limitations in terms of available space and material type and quantity allowed in a particular detector configuration. The thickness of the foil is determined by the commercially available dimensions, by mechanical stability arguments and by total material quantity allowed for the detector. The thickness of the gap between foils can be a limitation due to the difficulty to maintain the necessary regularity of the foil distances, especially for big collider detectors as ALICE.
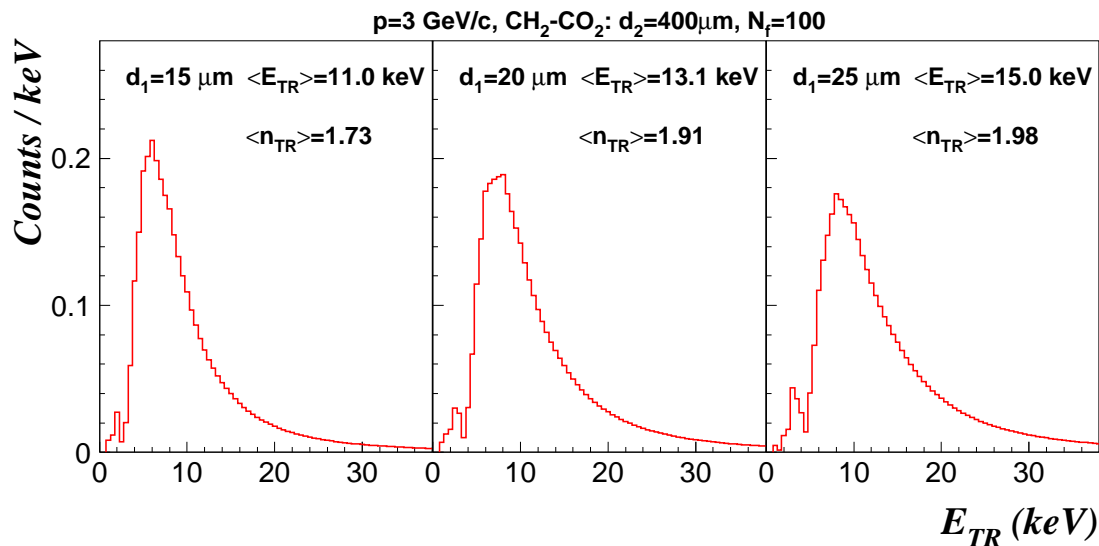


Figure 15: TR spectra for three values of the thickness of the radiator foil.

An example of the TR spectrum for three values of the thickness of the radiator foil ($d_1$=15, 20 and 25 $\mu$m) is presented in Fig. 15 for a $CH_2$-$CO_2$ radiator of 100 foils. The average values of the energy and of the number of TR photons are quoted as well and one can see the mentioned hardening of the spectra with increasing thickness.

The energy spectra of pions and electrons measured with the gas detector are presented

in Fig. 16 for one module. For the pions it represents the energy loss in the gas and has a typical Landau distribution. In the case of electrons it is the superposition of the energy loss and the signal produced by the absorption of the TR photons (in the present study only the total absorption is considered).
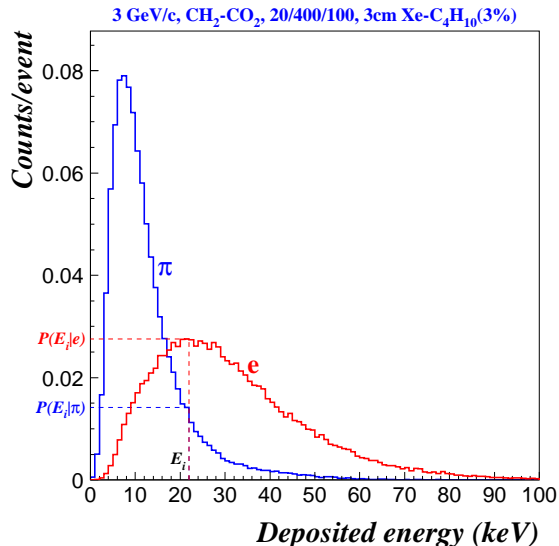


Figure 16: The spectra of total energy deposited in the gas detector for pions and electrons.
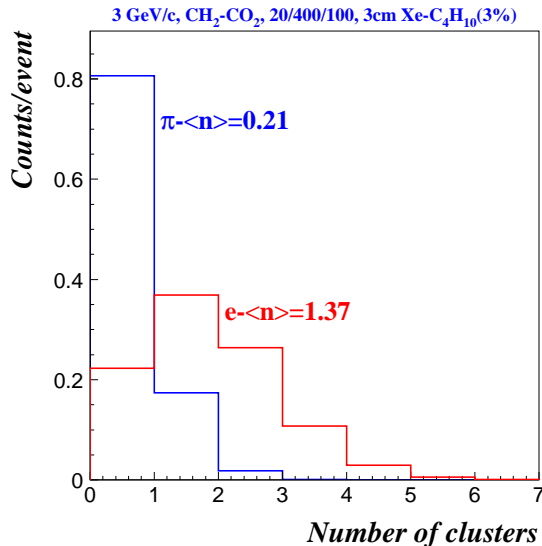
Figure 17: The distribution of the number of clusters above a threshold.

It is evident that due to the large tails in the energy loss spectrum for pions, the detector has to have many layers, and the discrimination is done using either a normal mean, a truncated mean (discarding the highest measured value of the detector sets) or better a likelihood method [14, 16, 38].

Taking these spectra (for each module) as probability distributions for electrons and pions to produce a signal of magnitude $E_i - P(E_i|e)$ and $P(E_i|\pi)$, respectively, as sketched in Fig. 16 – one constructs the **Likelihood** as [38]:

$$\text{Likelihood} = \sum_{i=1}^{N} \log \frac{P(E_i|e)}{P(E_i|\pi)} \tag{14}$$

or, equivalently [37]:

$$\text{Likelihood} = \frac{P_e}{P_e + P_\pi}, \quad P_e = \prod_{i=1}^{N} P(E_i|e), \quad P_\pi = \prod_{i=1}^{N} P(E_i|\pi) \tag{15}$$

where the sum (product) runs over the number of detector sets (modules). The quantities defined by formulas 14 and 15 are represented in Fig. 18 for both pion and electron, in the case of total charge likelihood. Both methods give obviously the same result on the pion rejection.

The pion misidentification probability ("pion efficiency") is the relative number of counts in the region defined by a certain electron efficiency (usually 90%, as sketched in Fig. 18 and in the following results).
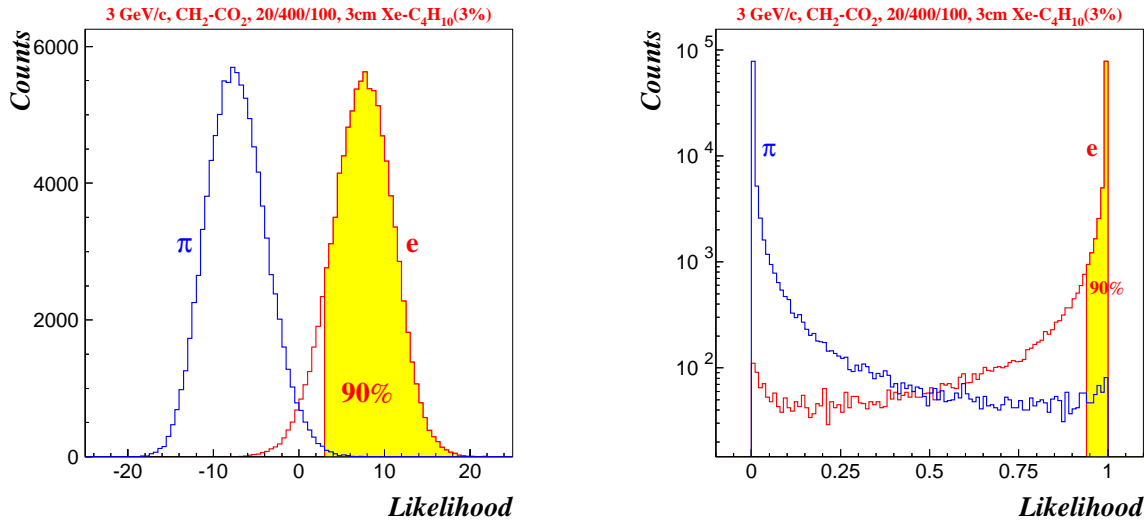
Figure 18: The distribution of the likelihood constructed from the spectra of Fig. 16 in the case of six detector modules, using definitions 14 - left panel and 15 - right panel.

As mentioned already, the cluster information, both on drift time and magnitude of the charge can contribute to improve the pion rejection. It was pointed out in ref. [34] that a bidimensional likelihood on cluster position and charge improves the rejection by a factor of 2 compared to the total charge likelihood.
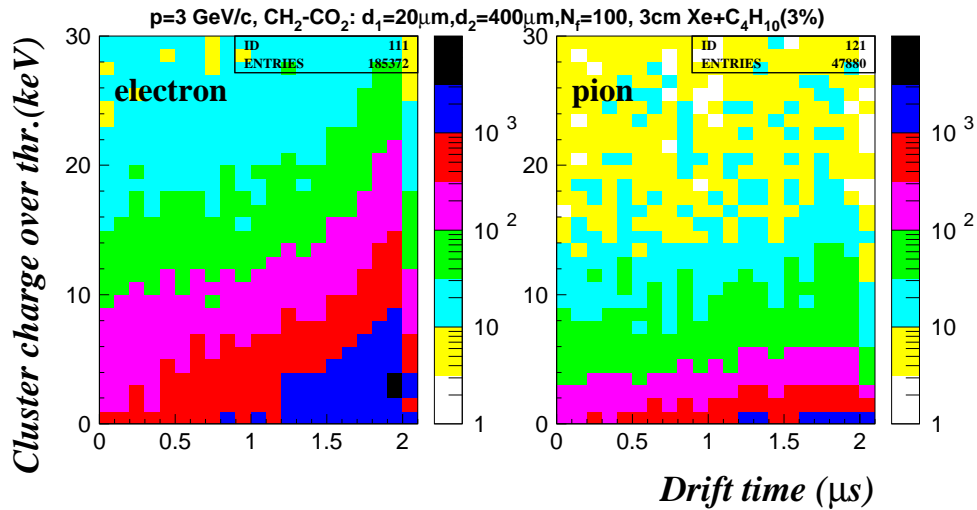


Figure 19: The distribution of the cluster charge above threshold as function of cluster position in the drift time.

Fig. 19 shows such bidimensional distributions for electron and pion and it is evident that there is a significant difference between these two particles.

It is not only the depth of the detector that determines its performance, the number of constituent modules and the method to process the signals play a significant role as well.
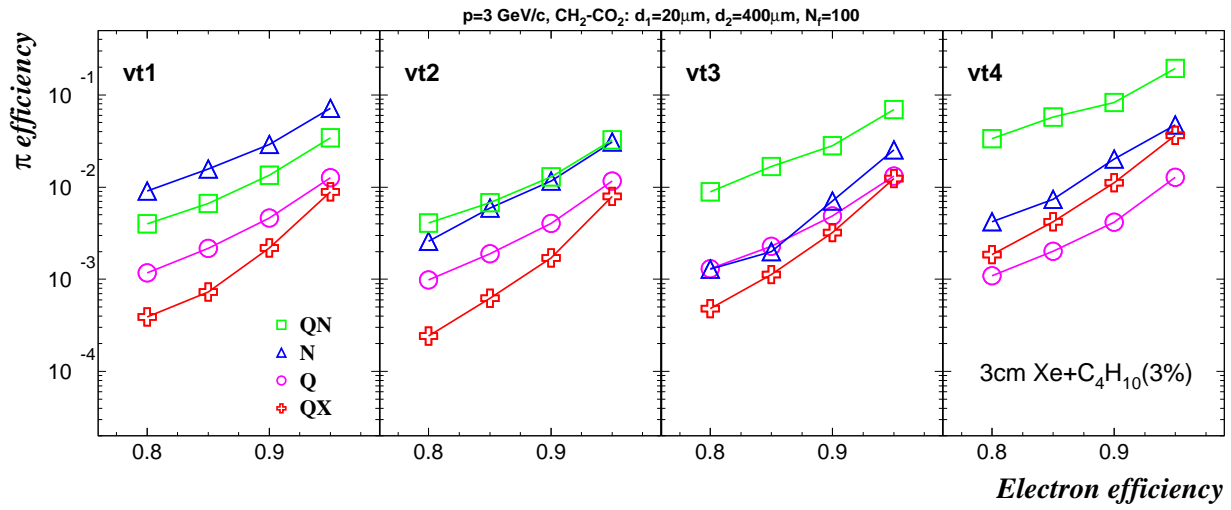
Figure 20: Pion misidentification probability as a function of electron efficiency for different methods of signal processing (see text for explanations).

To illustrate the last point, Fig. 20 shows as a function of the electron efficiency the pion misidentification probability derived (for a six layer detector) using four methods:

1) Q - likelihood on total charge, integrated above a certain low value threshold (10 times the noise level) [38], see Fig. 16;

2) N - likelihood on cluster number distribution. The clusters are counted if they are above a high value threshold [18], see Fig. 17;

3) QN - likelihood on total charge in the clusters [16];

4) QX - bidimensional likelihood taking into account the cluster charge above the threshold and cluster position in the drift time [34], see Fig. 19.

In general, the threshold used is a variable one. It increases as function of the drift time at which the cluster is found ("intelligent threshold" [18]). The four panels are obtained for different values of the threshold level, vt4 being the highest one. Depending on the method used, there is an optimum of the threshold value (vt2 for QX, vt3 for N). It is also evident that the QX method gives the best result, so that from here on we use this method (for the value vt2 of the threshold) to derive the optimum parameters of our detector.

Fig. 21 shows, as a function of the gap $d_2$ between the foils, the dependence of the average number $\langle n_{TR} \rangle$ of TR photons produced by electrons of 3 GeV/c momentum impinging perpendicular on a stack consisting of $N_f = 100$ foils in a $CO_2$ atmosphere for three values of the foil thickness $d_1 = 15$, 20 and 25 $\mu$m. The average number of produced TR photons in one foil stack starts to saturate at a foil spacing of around 500 $\mu$m. Also visible is that increasing the foil thickness from 20 to 25 $\mu$m the increase in TR production is quite small. In Fig. 22 is presented the corresponding pion misidentification probability assuming a six layer TRD. One can see that choosing gaps of 600 $\mu$m between the individual foils one can still improve the pion rejection factor. However, taking into account that keeping the required regularity of the foil separation might be more difficult for such a large foil gap and that the fibre radiator option would mean a lower TR production, we used the value $d_2 = 400$ $\mu$m for the subsequent studies of the pion misidentification probability. In terms of foil thickness,
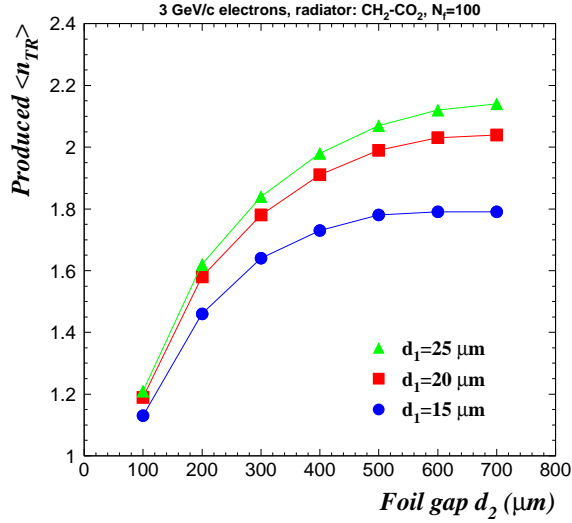
Figure 21: The dependence of TR production in one module on the foil spacing.
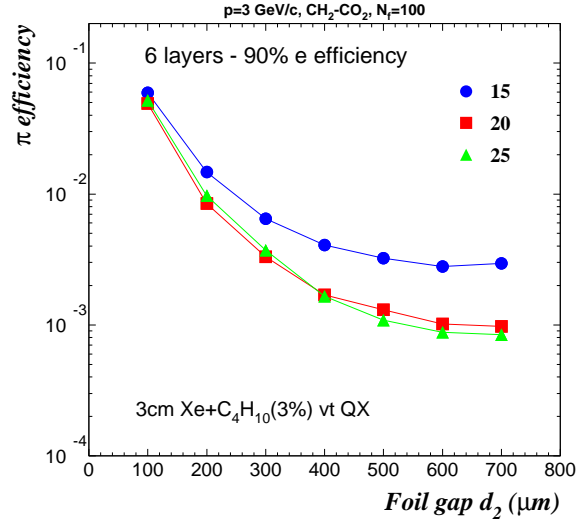
Figure 22: Pion efficiency as function of foil spacing for a 6 layer detector.

$d_1 = 20$ $\mu$m is an optimum, since the TR spectrum is harder for thicker foils and increasing $d_1$ further, the chamber gets more and more transparent for the TR photons.

Obviously, the overall depth of the gas volume should be large enough to ensure efficient X-ray absorption and to allow for a better pion rejection by exploiting the position information of the clusters. Also important is the total quantity of the gas (especially for expensive Xe) as well as other arguments, applicable to a particular implementation [20].
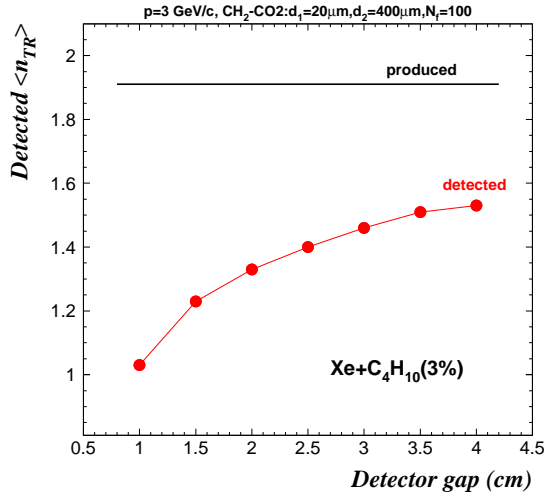




Figure 23: Average number of detected TR photons as function of gas thickness.
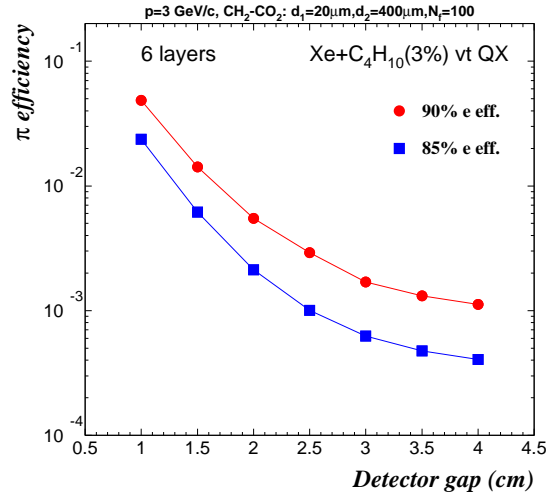
Figure 24: Pion rejection as function of TEC thickness.

Fig. 23 shows the simulated dependence of the average number of detected TR photons on the depth of the TEC gas volume for electron tracks normal to the TRD with a momentum

of 3 GeV/c (a foil of 25 $\mu$m mylar is considered as TEC gas barrier). It demonstrates that about 70% of the X-rays are absorbed already in the first 2 centimeters of the $Xe/C_4H_{10}$ mixture. Nevertheless, a deeper gas volume will clearly help to distinguish TR signals from fluctuations in the energy loss of charged particles by ionization (cf. Fig. 12), as shown in Fig. 24, which presents the pion misidentification probability for electron efficiencies of 90% and 85%, obtained with a 6 layer TRD. Increasing the depth of the TEC's drift region beyond 3 cm improves the TRD performance marginally, so for the moment we consider 3 cm as a desirable depth of the drift volume.
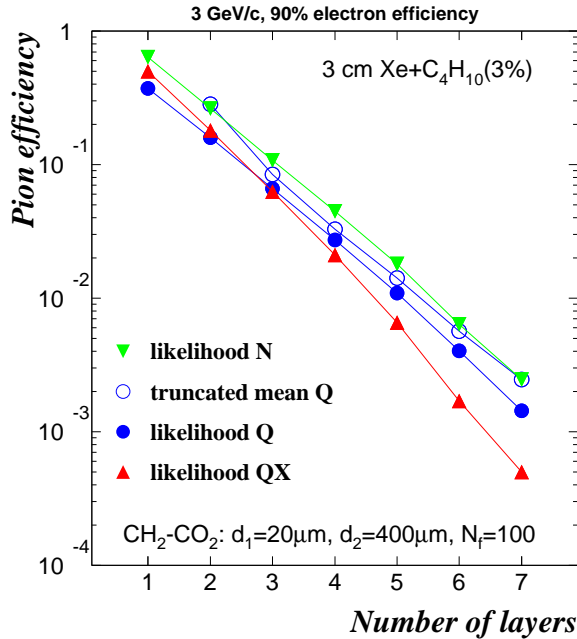


Figure 25: Pion rejection as function of number of modules.
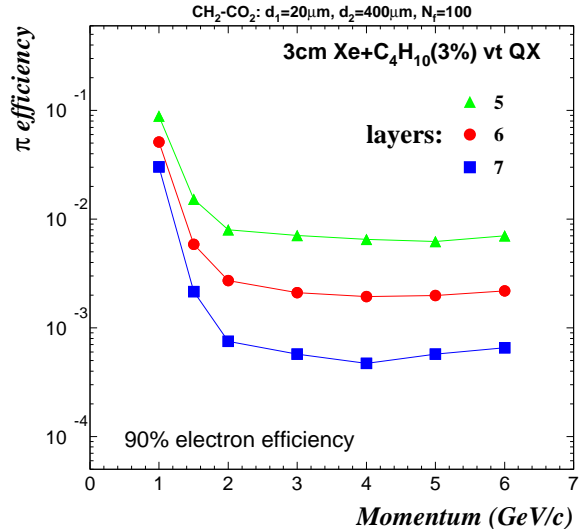
Figure 26: Momentum dependence of pion efficiency for 5, 6 and 7 identical layers TRD.

The dependence of the pion efficiency on the number of modules is shown in Fig. 25 for three methods mentioned above (Q, N and QX) to which the truncated mean on charge was added. As expected, the longer the better [39], but one can observe again that the method matters as well. The truncated mean on total charge gives only slightly worse results compared to the likelihood.

The dependence of the rejection power on the momentum of the incoming particle is shown in Fig. 26 for 5, 6 and 7 identical layers. In this representation the threshold character of the TR production is the reason behind the dramatic increase of the rejection power between 1 and 2 GeV/c. At higher momenta the pion misidentification is getting worse again due to the increase of the pion energy loss.

# 5   Conclusion

A simulation of a Transition Radiation Detector aiming to optimize the ALICE TRD has been performed. The results of this simulation show that the option with foil radiators

considered here has to have 6 sets of radiator (made out of 100 polypropylene foils of 20 $\mu$m thickness, separated by a gas layer of $\simeq$400 $\mu$m) and detector (2-3 cm Xe mixture).

# References

[1] V.L. Ginzburg and I.M. Frank, Zh. Eksp. Teor. Fiz. **16**, 15 (1946)

[2] G.M. Garibian, Nucl. Instr. and Meth. **125**, 133 (1975)

[3] M.L. Ter-Mikaelian, High Energy Electromagnetic Processes in Condensed Media, Wiley-Interscience, New York, 1972

[4] M.L. Cherry et al., Phys. Rev. D **10**, 3594 (1974)

[5] X. Artru et al., Phys. Rev. D **12**, 1289 (1975)

[6] L. Durand, Phys. Rev. D **11**, 89 (1975)

[7] C.W. Fabjan et al., Phys. Lett. B **57**, 483 (1975)

[8] C. Camps et al., Nucl. Instr. and Meth. **131**, 411 (1975)

[9] T.A. Prince et al., Nucl. Instr. and Meth. **123**, 231 (1975)

[10] J. Cobb et al., Nucl. Instr. and Meth. **140**, 413 (1977)

[11] C.W. Fabjan et al., Nucl. Instr. and Meth. **146**, 343 (1977)

[12] M.L. Cherry et al., Phys. Rev. D **17**, 2245 (1978)

[13] C.W. Fabjan et al., Nucl. Instr. and Meth. **185**, 119 (1981)

[14] A. Büngener et al., Nucl. Instr. and Meth. **214**, 261 (1983)

[15] R. Ansari et al., Nucl. Instr. and Meth. in Phys. Res. A **263**, 51 (1988)

[16] R.D. Appuhn et al., Nucl. Instr. and Meth. in Phys. Res. A **263**, 309 (1988)

[17] G.D. Barr et al., Nucl. Instr. and Meth. in Phys. Res. A **294**, 465 (1990)

[18] E. O'Brien et al., IEEE Trans. Nucl. Sc. **40**, 153 (1993)

[19] E. O'Brien et al., Nucl. Phys. A **566**, 615 (1993)

[20] B. Dolgoshein, Nucl. Instr. and Meth. in Phys. Res. A **326**, 434 (1993)

[21] J.-F. Detoeuf et al., Nucl. Instr. and Meth. in Phys. Res. A **265**, 157 (1988)

[22] H. Piekarz, Nucl. Instr. and Meth. in Phys. Res. A **367**, 220 (1995)

[23] G.E. Graham et al., Nucl. Instr. and Meth. in Phys. Res. A **367**, 224 (1995)

[24] H. Grässler et al., Nucl. Instr. and Meth. in Phys. Res. A **283**, 622 (1989)

[25] G.A. Beck et al., Nucl. Instr. and Meth. in Phys. Res. A **367**, 228 (1995)

[26] W. Brückner et al., Nucl. Instr. and Meth. in Phys. Res. A **378**, 451 (1996)

[27] M. Ambrosio et al., INFN/AE-97/04 (1997)

[28] T. Akesson et al., CERN PPE/97-161 (1997)

[29] G. Bassompierre et al., Nucl. Instr. and Meth. in Phys. Res. A **403**, 363 (1998)

[30] K. Ackerstaff et al., Nucl. Instr. and Meth. in Phys. Res. A **416**, 230 (1998)

[31] B. Dolgoshein et al., Nucl. Instr. and Meth. in Phys. Res. A **294**, 473 (1990)

[32] H.-J. Butt et al., Nucl. Instr. and Meth. in Phys. Res. A **252**, 483 (1986)

[33] Y. Watase et al., Nucl. Instr. and Meth. in Phys. Res. A **248**, 379 (1986)

[34] M. Holder and H. Suhr, Nucl. Instr. and Meth. in Phys. Res. A **263**, 319 (1988)

[35] M. Castellano et al., Comp. Phys. Comm. **51**, 431 (1988)

[36] M. Castellano et al., Comp. Phys. Comm. **61**, 395 (1990)

[37] R.D. Appuhn et al., Nucl. Instr. and Meth. in Phys. Res. A **270**, 387 (1988)

[38] G. Bassompierre et al., Nucl. Instr. and Meth. in Phys. Res. A **411**, 63 (1998)

[39] C. Caso et al., Eur. Phys. J. C **3**, 1 (1998)

[40] W.W.M. Allison and J.H. Cobb, Ann. Rev. Nucl. Part. Sc. **30**, 253 (1980)

[41] V.C. Ermilova et al., Nucl. Instr. and Meth. **145**, 555 (1977)

[42] F. Lapique and F. Piuz, Nucl. Instr. and Meth. **175**, 297 (1980)

[43] GEANT 3.21 Package, CERN Program Library W5013

[44] F. Sauli, CERN Report 77-09 (1977)

[45] W.Blum and L.Rolandi, Particle Detection with Drift Chambers, Springer-Verlag, 1994